

Synthesis of a Phased Array with Planar Near-Field Techniques Based on Far-Field Measurements of a Sub-Array in a CATR

Bernd Gabler, Diego Lorente
Microwaves and Radar Institute
German Aerospace Center (DLR)
82234 Oberpfaffenhofen, Germany
bernd.gabler@dlr.de

L.G.T. van de Coevering
March Microwave Systems B.V
5674 TM Nuenen, the Netherlands
vdcoevering@marchmicrowave.com

Abstract—Phased array antennas are often built from sub-arrays with identical or symmetrical layout. At an early project stage, performance verification measurements of the sub-array are valuable to proof the single module design. However, the characteristics of the final antenna are questionable without further processing. This work presents a concept that is based on far-field measurements of a sub-array in a Compact Antenna Test Range (CATR) in conjunction with planar near-field (PNF) processing to synthesize the entire phased array antenna characteristics. The procedure is explained with an example of a dual linear polarized L-band planar phased array antenna for an airborne synthetic aperture radar application. It is shown that the measured sub-array can be complemented by the synthesized twin to evaluate the characteristics of a final antenna that is not yet available in this form. The resulting performance of the synthesized entire phased array is presented and compared with simulations. The presented post-processing method would be beneficial to characterizing radiation patterns of large phased arrays by measuring only sub-arrays in a limited test-zone with any measurement principle.

I. INTRODUCTION

Phased array antennas achieve a high gain with a specific radiation pattern by arranging a set of single radiating elements in the available area. Their main technical benefit is the electrical beam steering capability by adjusting the phase difference of the element excitation signals in the feeding network. There is a huge demand to integrate new beam functionalities for commercial applications from the emerging mobile communication and IoT market into planar arrays, and from the military radar systems with their active electronically scanned arrays (AESA). In addition, it is required to continuously reduce physical size, weight and production cost. Depending on the application, stringent specifications create new challenges in the development to change proven designs and introduce different materials. The modular architecture of planar phased array antennas is advantageous to prove new developments with smaller units as the entire antenna. Already at an early project stage, measurements with smaller sub-arrays can be performed to verify the radiation properties. However, these characteristics are only valid for the sub-array, while a prediction for the final

radiation properties of the entire antenna would facilitate decisions for the subsequent project milestone.

A new dual linear polarized L-band phased array antenna is currently under development at the Microwaves and Radar Institute of the German Aerospace Center (DLR). It will be part of the next generation airborne SAR sensor F-SAR [1]. The beam is tilted 40° off nadir, while the antenna is mounted flat to one side of the fuselage. First, only half of the final array is manufactured to minimize prototyping cost. This sub-array features a ramp amplitude taper along azimuth and thus the shape of the beam is expected to be different from the full array with a triangular taper. Section II gives an insight into the design and the spherical measurements of the far-field pattern in the DLR Compact Test Range, a dual reflector CATR. Section III describes the processing scheme to reconstruct the missing half of the antenna. The measured spherical far-field pattern is transformed by expanding the spherical wave to the rectangular near-field geometry. By combining a virtual offset-shifted measurement with an identical but mirrored field, the full array can be synthesized. A planar near-field software module is used to transform this field distribution to far-field. Finally, the pattern of the complete phased array is compared with simulations.

II. DESCRIPTION OF THE AUT AND MEASUREMENTS

A. L-band Antenna Sub-Array Prototype

The new planar phased array L-band antenna for the future airborne SAR sensor is developed to operate at 1.325 GHz center frequency. A stacked dual patch configuration along with thick foam layers are used to achieve the design bandwidth of 150 MHz. To fulfill the performance requirements concerning beam shape and steering, the final antenna is built out of 5×8 array elements. However, the certified aircraft antenna mount offers only space for the current 4×6 elements array. Therefore, a highly compact single element design using truncated cavity-box stacked microstrip radiators is necessary. Dual linear polarized excitation of the square patches is provided by an aperture coupling network. This technique separates the feeding network from the radiating part and allows the design to be independent. The full phased array with a triangular amplitude

weighting in both azimuth and elevation will be built of two mirrored electrically identical sub-arrays, is schematically shown in Figure 1. A first sub-array prototype is manufactured for verification measurements of the radiation patterns.

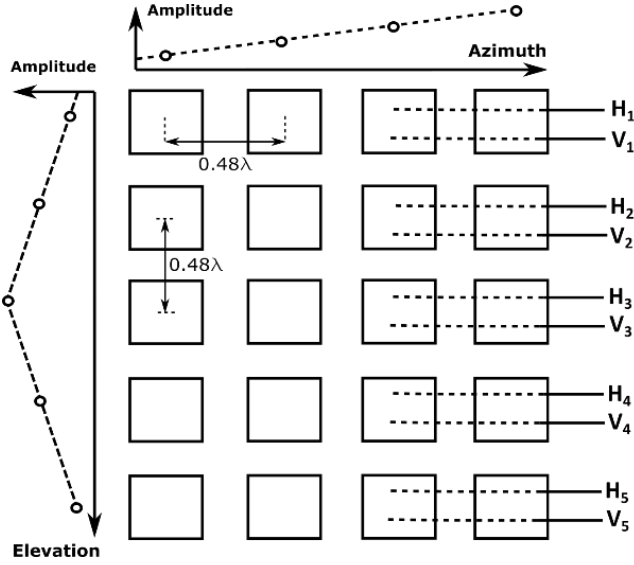


Figure 1. L-band 5x4 sub-array schematics.

B. Spherical Measurement in the CATR

Figure 2. shows the L-band sub-array mounted onto the positioner of the DLR Compact Test Range for spherical pattern characterization at both antenna polarization ports. The edges of the rectangular 543 mm x 652 mm structure are covered with RAM to match with simulations that use a radiation boundary airbox along the structure size. Swept frequency measurements are performed, covering 1.1 GHz to 1.7 GHz to enable an off-line time gating. Partial realized gain is obtained by applying the gain-transfer method and pattern integration gives the directivity of the antenna under test (AUT).

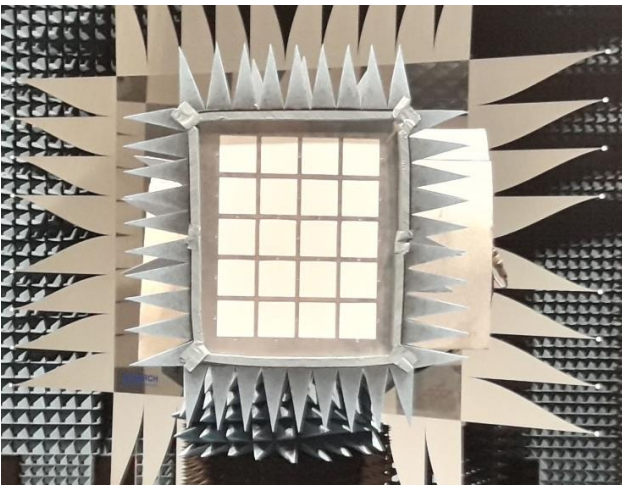


Figure 2. L-band 5x4 sub-array in the CATR

III. SYNTHESIS PROCESSING SCHEME

The electrical field vector in the near-field of the AUT is calculated by expansion of the spherical wave modes [2]. In this case, an XY-plane is generated at the virtual probe distance Z. Prior to the transformation, the origin of the measurement coordinate system is mathematically translated from the aperture plane to the field probe by differential phase shift. The far-field full spherical measurements confirm that the elevation feeding network is steering the beam around 40° to the side, which can be seen in Figure 3. for port 1 (horizontal polarization and port 2 (vertical polarization). Since a planar near-field scanner only almost captures a hemisphere [3], the conditions are certainly not ideal for the kind of AUT and need considerations about the alignment. It is advantageous to align the AUT maximum direction to the probe for reducing uncertainties in the region of interest. Similar to the real measurement world, an appropriate Euler rotation aligns the far-field measurement data in the spherical Ludwig II polarization basis. The computed near-field is then shifted and complemented with a mirrored copy. Subsequently, a planar near-field processing module transforms the resulting electrical fields back to a spherical far-field [4]. All measurement data processing was performed using ARCS Analysis [5].

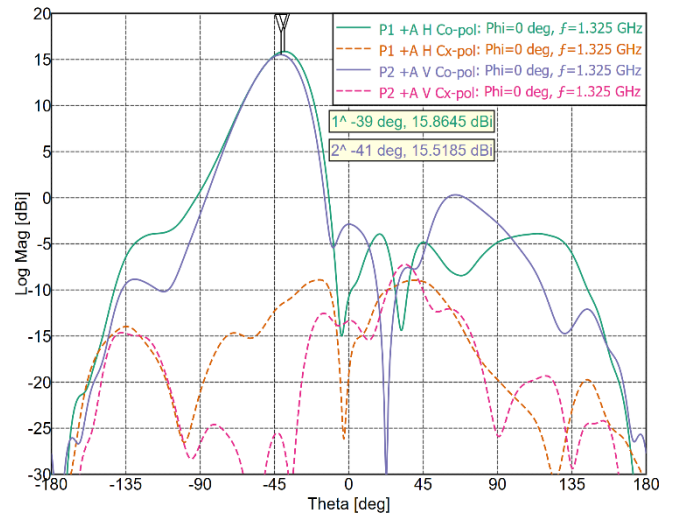


Figure 3. Sub-array far-field directivity elevation cuts

A. Theory

Transformation from spherical modes to a planar field is done using direct expansion of the base vectors with [2]

$$\vec{E}(\theta, \varphi, r) = \frac{k}{\sqrt{\zeta}} \sum_{s=1}^2 \sum_{n=1}^{\infty} \sum_{m=1}^{\infty} T_{smn} \vec{F}_{smn}^{(4)}(\theta, \varphi, r). \quad (1)$$

In (1) k is the wave number and ζ the impedance of free space. The spherical wave coefficients T are obtained from the far-field with the procedure outlined in [2]. $\vec{F}_{smn}^{(4)}$ are the spherical basis functions:

$$\begin{aligned}
\vec{F}_{1mn}^{(4)}(\theta, \varphi, r) &= -\frac{1}{\sqrt{2\pi}} \frac{1}{\sqrt{n(n+1)}} \left(-\frac{m}{|m|}\right)^n h_n^{(2)}(kr) e^{-jm\varphi} \\
&\quad \left\{ \frac{jm}{\sin\theta} \overline{P}_n^{|m|}(\cos\theta) \vec{e}_\theta + \frac{d}{d\theta} \left(\overline{P}_n^{|m|}(\cos\theta) \right) \vec{e}_\varphi \right\} \\
\vec{F}_{2mn}^{(4)}(\theta, \varphi, r) &= \frac{1}{\sqrt{2\pi}} \frac{1}{\sqrt{n(n+1)}} \left(-\frac{m}{|m|}\right)^n e^{-jm\varphi} \\
&\quad \left\{ h_n^{(2)}(kr) \frac{n(n+1)}{kr} \overline{P}_n^{|m|}(\cos\theta) \vec{e}_r \right. \\
&\quad \left. + \frac{1}{kr} \frac{d}{d(kr)} \left(kr h_n^{(2)}(kr) \right) \right. \\
&\quad \left. \left[\frac{d}{d\theta} \left(\overline{P}_n^{|m|}(\cos\theta) \right) \vec{e}_\theta + \frac{jm}{\sin\theta} \left(\overline{P}_n^{|m|}(\cos\theta) \right) \vec{e}_\varphi \right] \right\}
\end{aligned} \quad (2)$$

with $\overline{P}_n^{|m|}$ the Normalized Associated Legendre functions and $h_n^{(2)}$ the Hankel function of the second kind. In comparison with the Fourier based expansion method that is used for the far-field direct application of (2) is costly. In order to speed up the processing precomputation and vectorization as described in [6] is applied. Additionally, calculation of multiple points is inherently parallel. A further complication is the fact that the imaginary part of the Hankel function $h_n^{(2)}$ is infinite at the origin. Although this is perfectly fine in spherical near-field applications because the modal expansion (1) is not valid for $n < kr$, this would forbid a small z in the current application. At present the imaginary part of $h_n^{(2)}$ is set to zero whenever $n < kr$.

Note that (1) is Theta-Phi both in coordinate system and polarization basis. All evaluated points are needed in a Ludwig-I basis and both pre- and post-conversions are necessary [2][7]. The required origin translation in the (x,y,z)-direction is simplest in the far-field with

$$\begin{aligned}
\vec{E}(\Delta_x, \Delta_y, \Delta_z, \theta, \varphi) &= \\
\vec{E}(\theta, \varphi) e^{j(\Delta_x \sin\theta \cos\varphi + \Delta_y \sin\theta \sin\varphi + \Delta_z \cos\theta)}, & \quad (3)
\end{aligned}$$

where $\Delta_{\{x,y,z\}}$ is the desired offset shift. Rotation of the far-field can be realized with resampling in the angular domain or by applying the rotation operator to the spherical modes [2].

The thus obtained planar near-field data is transformed to the angular spectrum \vec{F}_T using [4]

$$\vec{F}_T(k_x, k_y) = \iint (E_x \vec{e}_x + E_y \vec{e}_y) e^{j(k_x x + k_y y)} dx dy. \quad (4)$$

Only the x and y Ludwig-I components are applied as would be in a standard planar near-field measurement. No probe correction is required and the far-field tangential components are calculated with

$$\vec{E}_{ff}(k_x, k_y) = j \frac{\sqrt{1-k_x^2-k_y^2}}{\lambda} \vec{F}_T(k_x, k_y). \quad (5)$$

Obviously, in (5) k_x and k_y are inside the unit circle and after realizing that this is a projection of the forward hemisphere, transformation to other coordinate systems and polarization definitions is possible.

Directivity calibration of the resulting antenna pattern is achieved by integration of the far-field pattern \vec{E}_{ff} in (5) over the unit circle.

B. Proof of Concept

After the conditioning of the measurement data, an intermediate step is introduced: To confirm the validity of this method, the near-field of the sub-array only is transformed back to far-field for comparison with the original measurement results. The color-coded contour plot of the total E-field in Figure 4. displays the ramp amplitude distribution from the sub-array azimuth feeding network in Y-direction and the elevation triangular weighting network in X-direction

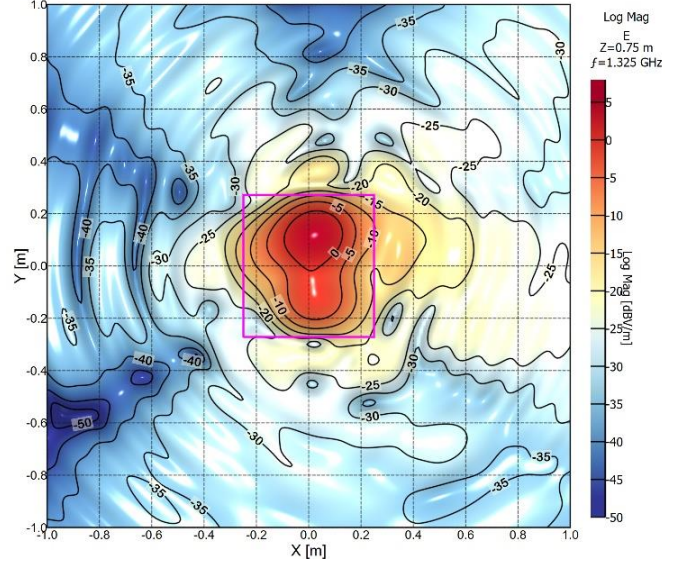


Figure 4. Port 1 total E-field, Z=0.75m, sub-array outline in purple color

The planar near-field to far-field transformation initially generates values that cover almost a hemisphere, in this case centered to the maximum direction of the beam. In the reconstructed far-field pattern of Figure 5. , a rotation back to the original boresight direction and a transformation to azimuth over elevation coordinates that is more convenient for the SAR application, is applied. Compared with the measurements, there is a good similarity in wide areas. The error pattern in Figure 6. shows that this is especially true in main beam direction. With elevation angles approaching $\pm 90^\circ$, corresponding to the direction of the horizon for the airborne SAR application, increasing errors are insignificant. At the low levels of the cross-polarization, small changes cause a large impact. The difference between measured and reconstructed cross polar levels is plotted in Figure 7. , and remains within an acceptable margin. The same applies for the phase. A singularity in the Ludwig-II coordinates that appears as discontinuity in Z-direction is considered by a Burg estimation [8].

In consequence, this proof of concept demonstrates that the procedure can be considered reliable with limitations coming from the beam steering of the example AUT. Subsequently, the method is applied to synthesize the full array out of the sub-array measurement.

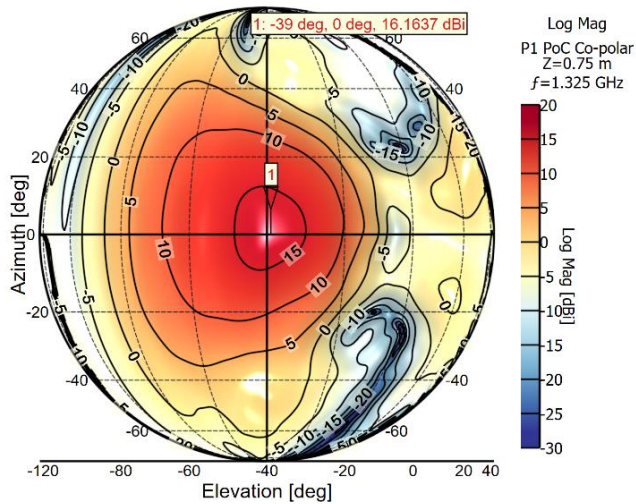


Figure 5. Port 1 co-polar reconstructed far-field

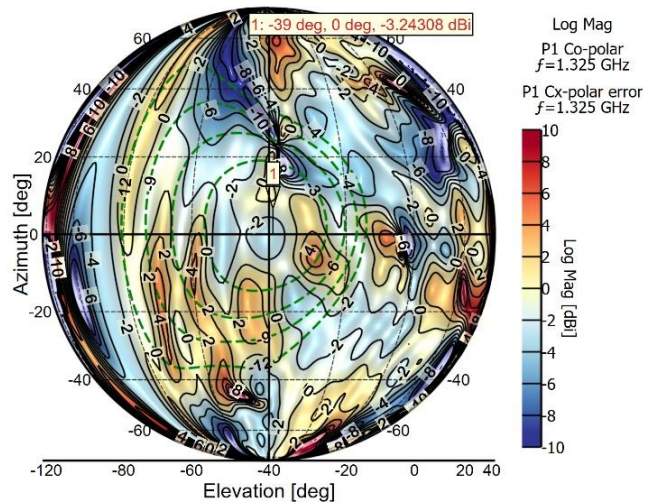


Figure 7. Port 1 cross-polar, differential pattern of the measured vs. the reconstructed, with norm. co-polar contour overlay in dashed green, -3 dB steps

C. Synthesis of the full array

The full array is built of two electrically identical mirrored sub-arrays, side by side. To follow this numerically, first the origin of the measurement coordinate system is mathematically translated from the aperture plane to the field probe and moved out of center in Y-direction by differential phase shift. A second identical but mirrored dataset is generated that represents the missing half sub-array. Both datasets are added, resulting in the near-field of Figure 8. With the complemented virtual twin, the asymmetric sub-aperture amplitude weighting along the Y-axis is largely compensated. Following the description of the method, this full array planar near-field dataset is transformed to far-field, and subsequently the maximum is translated back to the original position. The corresponding spherical orthographic plot is provided in Figure 9.

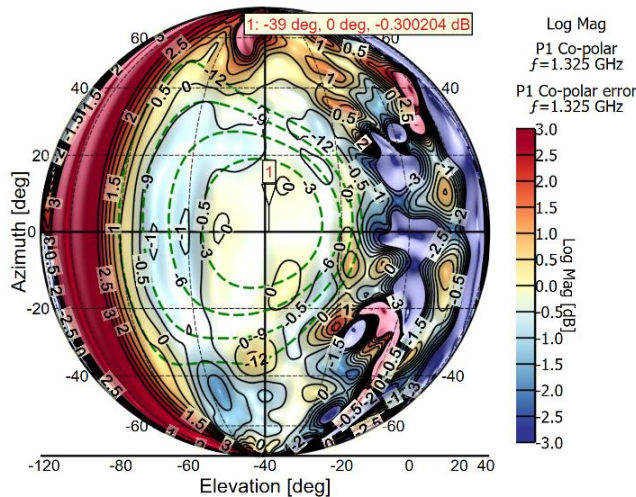


Figure 6. Port 1 co-polar, differential pattern of the measured vs. the reconstructed, normalized co-polar contour overlay in dashed green, -3 dB steps

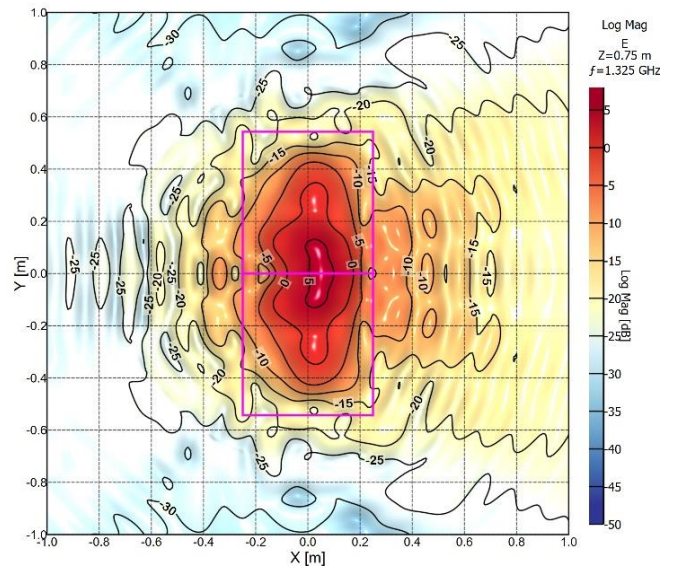


Figure 8. Port 1 total E-field, synthesized full array, $Z=0.75$ m outline in purple color

IV. VALIDATION BY COMPARISON WITH SIMULATIONS

A comparison of the elevation cuts of the synthesized full array with simulation results from Ansys HFSS is shown in Figure 10. for port 1 and in Figure 11. for port 2. There is a good similarity for the co-polar in the relevant angular range for the SAR application between -20° and -70° , while -90° corresponds to the horizontal and does not contribute to the remote sensing information. High magnitudes from smaller absolute angular directions are towards the nadir direction that are gated out in the

image, but still critical because of potential saturation of the receiver. The measured cross-polar levels of port 1 are remarkably higher than those of port 2. Since the synthesis method is directly connected to the measurements, a considerable improvement was not expected. At both ports, the disagreement with respect to the simulation is closely coupled with AUT manufacturing inaccuracies and the cross-polar measurement capabilities.

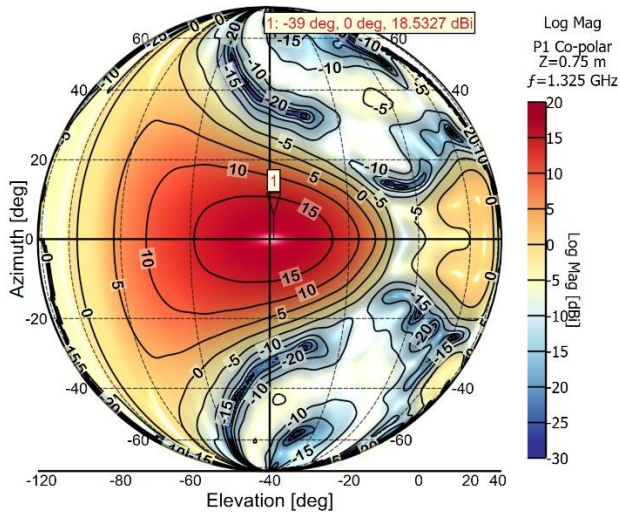


Figure 9. Port 1 co-polar, synthesized full array

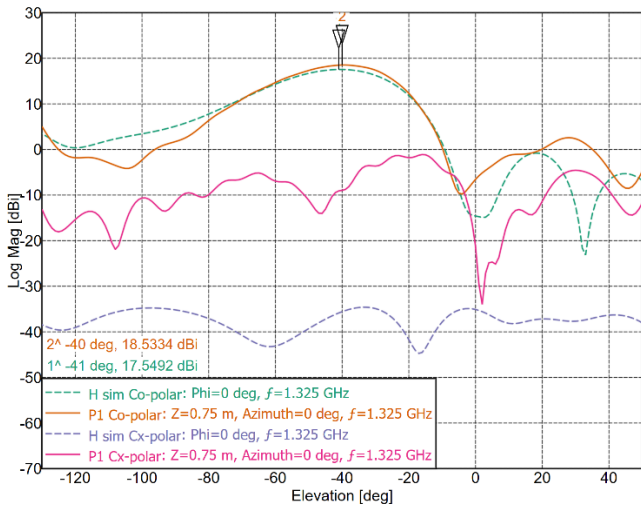


Figure 10. Port 1 synthesized full array in solid lines, simulated in dashed lines

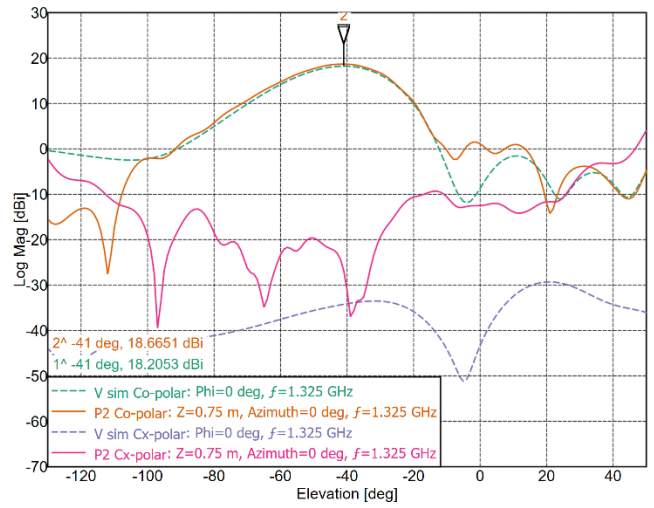


Figure 11. Port 2 synthesized full array in solid lines, simulated in dashed lines

V. CONCLUSION

The example with the side-looking SAR antenna illustrates the potential and limits of the method for today's beam steering applications. It is demonstrated that a planar array can be synthesized from the measurement data of a single element by use of spherical and planar techniques. Possible improvements in the presented technique are the use of E_z in the planar transformation and application of the spherical mode translation operator to calculate the field inside the $n=kr$ circle.

REFERENCES

- [1] D. Lorente, M. Limbach and B. Gabler, "L-Band Antenna Array for Next Generation DLR Airborne SAR Sensor," 12th German Microwave Conference (GeMiC), IEEE 2019, pp. 182-185.
- [2] Hansen (ed), Spherical Near-Field Antenna Measurements. Peter Peregrinus Ltd. 1988.
- [3] S. Gregson, J. McCormick, D. J. Van Rensburg, and C. Parini, Theory and Practice of Modern Antenna Range Measurements. London, U.K.: The Institution of Engineering and Technology, 2014.
- [4] S. Gregson, J. McCormick, and C. Parini, Principles of Planar Near-Field Antenna Measurements.. London, U.K.: The Institution of Engineering and Technology, 2007.
- [5] ARCS Analysis Manual v1.74, Nuenen, the Netherlands, March Microwave Systems, September 2020
- [6] T. Limpanuparb, J. Milthorpe, "Associated Legendre Polynomials and Spherical Harmonics Computation for Chemistry Applications" Proceedings of The 40th Congress on Science and Technology of Thailand; 2014, <https://arxiv.org/abs/1410.1748>.
- [7] A.C. Ludwig, "The definition of Cross-polarization", IEEE Trans. Antennas Propagation, vol. AP-21 no 1, pp. 116-9, Jan. 1973.
- [8] S.M. Kay, "Modern Spectral Estimation, Theory and Application," . Englewood Cliffs, NJ, Prentice Hall, Jan. 1988.